




## Spin and valley polarization of an MoS<sub>2</sub> zigzag nanoribbon with a magnetic barrier via Fano resonance

Daehan Park  and Nammee Kim \**Department of Physics, Soongsil University, Seoul 06978, Korea* (Received 3 August 2022; revised 2 December 2022; accepted 2 December 2022; published 14 December 2022)

For monolayer MoS<sub>2</sub>, a magnetic field causes the degeneracy of the  $K$  and  $K'$  valleys to be lifted, owing to the valley Zeeman effect. Thus, in a monolayer MoS<sub>2</sub> nanoribbon system with a magnetic barrier, electrons in these valleys exhibit different conductance behaviors when passing through the barrier. One valley shows a strong dip in conductance caused by Fano resonance, i.e., quantum interference between continuum states and Landau levels in the magnetic barrier. This dip can be modulated by changing the strength and length of the magnetic barrier. By calculating the asymmetric conductance for the  $K$  and  $K'$  valleys as a function of incident energy with various values of the physical parameters, optimized conditions for spin and valley polarization can be found. The results presented here provide useful information to enable implementation of spin- and valley-polarized currents in future devices.

DOI: [10.1103/PhysRevB.106.235123](https://doi.org/10.1103/PhysRevB.106.235123)

### I. INTRODUCTION

Since the realization of monolayer graphene [1], there has been extensive research on 2D materials. Among such materials, transition metal dichalcogenides (TMDCs) have been widely investigated, owing to their peculiar physical properties [2]. These properties open the way to possible device applications such as Field Effect Transistors (FETs) at room temperature [3], Light Emitting Diodes (LEDs) [4], photodetectors [5], and gas sensors [6]. TMDCs have the general formula  $MX_2$ , where  $M$  is a transition metal in group IV and  $X$  is a chalcogen element.

Monolayer MoS<sub>2</sub>, an example of a TMDC, has a direct band gap of 1.8 eV at the  $K$  and  $K'$  points [7], whereas bulk MoS<sub>2</sub> has an indirect band gap of 1.2 eV [8]. One of the features of these TMDCs is very strong spin-orbit interaction (SOI); in particular, the intrinsic SOI of MoS<sub>2</sub> is about 150 meV [9]. Similar to graphene, MoS<sub>2</sub> has a conduction band minimum and valence band maximum at the  $K$  and  $K'$  points in the first Brillouin zone. These two points are degenerate and related by time-reversal symmetry. Owing to the large momentum separation between the  $K$  and  $K'$  valleys, intervalley scattering is suppressed [10]. Therefore, the valleys can be considered as representing an additional degree of freedom similar to the spin degree of freedom. Threefold rotations and intrinsic inversion symmetry breaking give rise to interesting phenomena associated with the valleys, such as the valley Hall effect [11] and valley optical selection rules [2,12–14]. Manipulating this valley degree of freedom has led researchers to explore so-called valleytronics [15].

One of the important issues that arise in the quest to realize valleytronics is the control of valley polarization, i.e., the relative population ratio between the  $K$  and  $K'$  valleys. Typically, this valley polarization can be manipulated by a magnetic field [16,17], an electric field [18–20], strain [21], optical pumping with circularly polarized light [14,22,23], and a valley magnetoelectric effect [20]. With regard to applications of valleytronics based on MoS<sub>2</sub>, diverse models and devices have been proposed theoretically. For instance, a normal/ferromagnetic/normal (NFN) MoS<sub>2</sub> junction has been reported to control spin and valley polarization by controlling gate voltage [24,25]. It has also been found that with the application of circularly polarized light, ferromagnetic materials on monolayer MoS<sub>2</sub> are able to generate high spin and valley polarization [26,27]. Liu *et al.* [28] examined how strain on NFN monolayer MoS<sub>2</sub> affected spin and valley polarization. For a system consisting of an array of ferromagnetic materials on MoS<sub>2</sub>, valley-resolved conductance oscillations were observed by modulation of its gate voltage [29]. Ferromagnetic/superconductor/ferromagnetic [30], normal/superconductor [31], and ferromagnetic/insulator/normal/ferromagnetic [32] structures have also been reported.

Among interesting properties related to the valley, TMDCs, including MoS<sub>2</sub>, exhibit the so-called valley Zeeman effect, which is analogous to the ordinary Zeeman effect. In the valley Zeeman effect, an applied magnetic field causes energies between valleys to be lifted and split. As with the valley Hall effect and valley optical selection rules, it is the broken inversion symmetry of the TMDCs that is responsible for the valley Zeeman effect [17]. This effect has been studied experimentally [33–36] and theoretically [37] in various TMDCs.

In this paper, we propose that valley polarization can be achieved by Fano resonance in a zigzag nanoribbon (ZNR) system with a magnetic barrier, basing our work on a three-band model for MoS<sub>2</sub>. Fano resonance is a general wave phenomenon caused by wave interference between a continuum state and a bound state. This interference results in

\*nammee@ssu.ac.kr

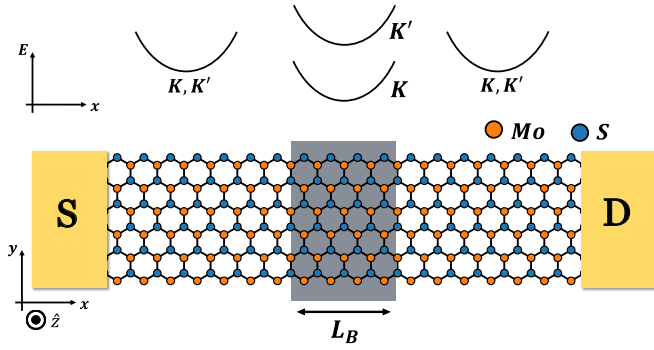


FIG. 1. Schematic geometry of a MoS<sub>2</sub> zigzag nanoribbon with a magnetic barrier [ $\vec{B} = B(x)\hat{e}_z$ ]. The magnetic barrier with length  $L_B$  is represented by the gray region. The curves at the top of the figure indicate the energy dispersion of the  $K$  and  $K'$  valleys in nonmagnetic and magnetic barrier regions.

asymmetric line shapes, which can be observed in quantum transport processes, including those in Aharonov–Bohm interfaces [38], quantum dots [39], cavities [40], and spintronics [41–44]. In the system illustrated in Fig. 1, we will show valley polarization by calculating the asymmetric conductance within the Landauer–Büttiker formalism. The  $K$  and  $K'$  valleys exhibit different behaviors in magnetic fields, owing to the valley Zeeman effect in the magnetic barrier region, which is represented by the gray region of length  $L_B$  in Fig. 1. As a result of the valley Zeeman effect, Landau levels (LLs) of one of the valleys are lowered as the magnetic field increases. These LLs interact with continuum states, resulting in a dip in conductance, i.e., there is strong backscattering caused by Fano resonance. In this strong conductance dip, an electron in another valley can propagate through the magnetic barrier without being totally suppressed. In this process, a fully valley-polarized current can be obtained. Furthermore,

we will touch on the possibility of spin- and valley-polarized devices.

The remainder of this paper is organized as follows. In Sec. II, we introduce a mathematical model for calculating transport properties of the  $K$  and  $K'$  valleys in our system. In Sec. III, we present our numerical results for the conductance of the  $K$  and  $K'$  valleys and the spin and valley polarization. Finally, in Sec. IV, we summarize our main results.

## II. MATHEMATICAL MODEL

Monolayer MoS<sub>2</sub> is made up of one layer of Mo and two layers of S atoms. From first-principles calculations [45–47], it has been shown that the electronic bands of MoS<sub>2</sub> in the  $K$  and  $K'$  valleys near the Fermi energy are mainly composed of three  $d$  orbitals ( $d_{xy}$ ,  $d_{x^2-y^2}$ ,  $d_{z^2}$ ) of Mo atoms. A three-band tight-binding model (TBM) of MoS<sub>2</sub> provides a good description of the properties of the  $K$  and  $K'$  valleys and the edge states near the Fermi energy [45], and so such a model is chosen for our calculations. The corresponding tight-binding Hamiltonian is

$$H = \sum_{i,\mu} \epsilon_{i,\mu}^{\text{Mo}} c_{i,\mu}^\dagger c_{i,\mu} + \sum_{\langle i,j \rangle} \sum_{\mu,\nu} t_{i\mu,j\nu}^{\text{Mo-Mo}} c_{i,\mu}^\dagger c_{j,\nu}, \quad (1)$$

where  $c_{i,\mu}$  and  $c_{i,\mu}^\dagger$  are, respectively, annihilation and creation operators of electrons on  $d$  orbital  $\mu$  for MoS<sub>2</sub> at site  $i$ . Here,  $\langle i,j \rangle$  indicates that the summation runs over all nearest-neighbor atoms. The on-site energy  $\epsilon_{i,\mu}^{\text{Mo}}$  and hopping parameters  $t_{i\mu,j\nu}^{\text{Mo-Mo}}$  can be written in matrix form as follows:

$$\epsilon^{\text{Mo}} = \begin{pmatrix} \epsilon_1 & 0 & 0 \\ 0 & \epsilon_2 & i\lambda_M s_z \\ 0 & -i\lambda_M s_z & \epsilon_3 \end{pmatrix}, \quad (2)$$

$$t_E^{\text{Mo-Mo}} = \begin{pmatrix} t_0 & t_1 & t_2 \\ -t_1 & t_{11} & t_{12} \\ -t_2 & -t_{12} & t_{22} \end{pmatrix}, \quad (3)$$

$$t_{NE}^{\text{Mo-Mo}} = \begin{pmatrix} t_0 & -\frac{1}{2}t_1 + \frac{\sqrt{3}}{2}t_2 & -\frac{\sqrt{3}}{2}t_1 - \frac{1}{2}t_2 \\ \frac{1}{2}t_1 + \frac{\sqrt{3}}{2}t_2 & \frac{1}{4}t_{11} + \frac{3}{4}t_{22} & \frac{\sqrt{3}}{4}(t_{11} - t_{22}) + t_{12} \\ \frac{\sqrt{3}}{2}t_1 - \frac{1}{2}t_2 & \frac{\sqrt{3}}{4}(t_{11} - t_{22}) - t_{12} & \frac{3}{4}t_{11} + \frac{1}{4}t_{22} \end{pmatrix}, \quad (4)$$

$$t_{NW}^{\text{Mo-Mo}} = \begin{pmatrix} t_0 & \frac{1}{2}t_1 - \frac{\sqrt{3}}{2}t_2 & -\frac{\sqrt{3}}{2}t_1 - \frac{1}{2}t_2 \\ -\frac{1}{2}t_1 - \frac{\sqrt{3}}{2}t_2 & \frac{1}{4}t_{11} + \frac{3}{4}t_{22} & -\frac{\sqrt{3}}{4}(t_{11} - t_{22}) - t_{12} \\ \frac{\sqrt{3}}{2}t_1 - \frac{1}{2}t_2 & -\frac{\sqrt{3}}{4}(t_{11} - t_{22}) + t_{12} & \frac{3}{4}t_{11} + \frac{1}{4}t_{22} \end{pmatrix}, \quad (5)$$

where  $s_z = \pm 1$  is the  $z$  component of the spin degree of freedom. The values of the parameters used in the three-band model are shown in Table I.

Based on the three-band TBM, an MoS<sub>2</sub> ZNR of width 60 nm with a magnetic barrier is considered. The magnetic field describing this barrier is given by

$$\vec{B}(x) = B \left[ \theta \left( x - \frac{L_B}{2} \right) - \theta \left( x + \frac{L_B}{2} \right) \right] \hat{e}_z, \quad (6)$$

where  $\theta(x)$  is the Heaviside function, and  $L_B$  and  $B$  are, respectively, the length and strength of a single magnetic barrier.

The corresponding vector potential is  $\vec{A} = (0, A_y, 0)$ , with

$$A_y = B_0 \left[ \left( x + \frac{L_B}{2} \right) \theta \left( x + \frac{L_B}{2} \right) - \left( x - \frac{L_B}{2} \right) \theta \left( x - \frac{L_B}{2} \right) \right]. \quad (7)$$

To include the magnetic field in the three-band TBM, the hopping terms are modified by multiplying by the Peierls phase  $\theta_P$ :  $t \rightarrow e^{i\theta_P} t$ , where the Peierls phase is defined by  $\theta_P = (e/\hbar) \int_1^2 \vec{A} \cdot \vec{dl}$ . In our case, the Peierls phase

TABLE I. Parameters of three-band model [45].

Parameter	Value
$\epsilon_1$	1.046
$\epsilon_2$	2.104
$t_0$	-0.184
$t_1$	0.401
$t_2$	0.507
$t_{11}$	0.218
$t_{12}$	0.338
$t_{22}$	0.057
$\lambda_M$	0.073

becomes

$$\theta_p = \frac{B_0 y_2 - y_1}{2 x_2 - x_1} \left[ f\left(x_2, \frac{L_B}{2}\right) - f\left(x_1, \frac{L_B}{2}\right) - f\left(x_2, -\frac{L_B}{2}\right) + f\left(x_1, -\frac{L_B}{2}\right) \right], \quad (8)$$

where  $f(x, y) = (x + y)^2 \theta(x + y)$ .

KWANT, an open-source Python package [48], is used in our simulation. In this program, within the Landauer–Büttiker formalism, the conductance  $G = (e^2/h) \sum T_{ij}$ , where  $T_{ij}$  is a transmission coefficient from the  $i$ th channel to the  $j$ th channel. This software program has been applied to numerous quantum transport problems with high accuracy and reasonable computation times. Basing our study on the three-band TBM with KWANT, we will focus on quantum transport properties of conduction bands in the  $K$  and  $K'$  valleys.

### III. RESULTS AND DISCUSSION

As is well-known, the degeneracy of the  $K$  and  $K'$  valleys is broken when a magnetic field is applied. In Fig. 2, the energy band structure of conduction electrons of an MoS<sub>2</sub> ZNR is shown in the case of uniform magnetic fields. The energy splitting called the valley Zeeman effect is illustrated well in Fig. 2(a) for a 10 T magnetic field. As the magnetic field increases, the valley Zeeman effect becomes larger and the parabolic bottom shapes of energy states change to flat. Note that in this three-band model, zero energy is defined at the valence band maximum [45]. Figure 2(b) shows the energy dispersion of an MoS<sub>2</sub> ZNR of width 60 nm as a function of magnetic field. The solid and dashed lines indicate the LLs at the  $K$  and  $K'$  valleys, respectively. For simplicity, we draw the LLs without the spin splitting in this figure. The splitting of LLs between the two valleys is enhanced when the magnetic field increases, as we know. One interesting point is that for our sample size, the zeroth LL of the  $K$  valley decreases as the magnetic field increases. However, as shown in Fig. 2(c), the energy differences between the zeroth LL and the other LLs is the same for both valleys. This means that the energy spacing between the valleys remains the same, i.e., the energy shift between the two valleys due to the valley Zeeman effect is constant. Because of this valley Zeeman effect, when electrons move from source to drain, they are affected differently by the magnetic field, depending on their valleys. We now turn in Secs. III A and III B to consider how conduction electrons

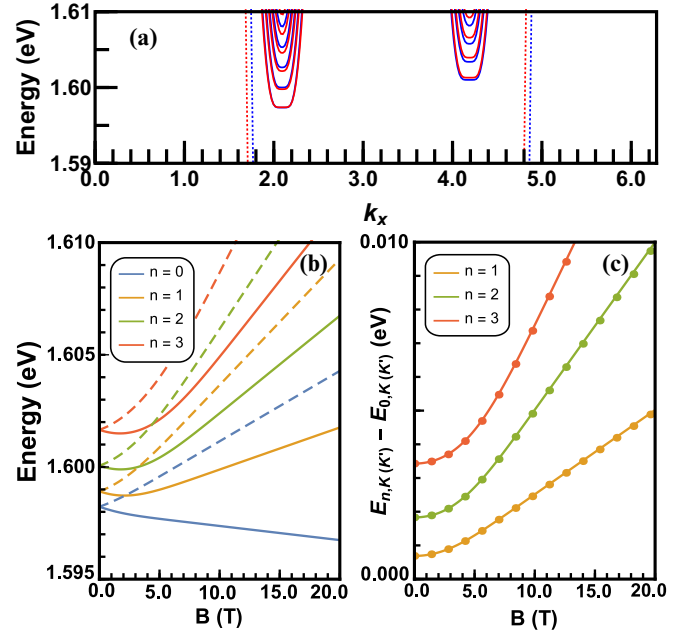


FIG. 2. (a) Energy dispersion of an MoS<sub>2</sub> ZNR at 10 T near the conduction band including the spin-orbit interaction. The blue (red) lines indicate the spin-up (spin-down) states and the dotted lines indicate the intrinsic edge states of the system. (b) Landau levels for both the  $K$  (solid lines) and  $K'$  (dashed lines) valleys. (c) Energy differences between the zeroth Landau level and the other Landau levels for the  $K$  (solid lines) and  $K'$  (filled circles) valleys.

in the  $K$  and  $K'$  valleys are affected by the magnetic barrier in our system. On this basis, we will discuss the valley and spin polarizations of the system in Sec. III C. From now on, we assume that the energy  $E_F = E_{3\text{band}} - 1.5975$  eV, where  $E_{3\text{band}}$  is the energy calculated from the three-band model. Also, from our numerical calculation, the ratio of intervalley transitions to intravalley transitions is about  $10^{-10}$ , and so we ignore intervalley transitions in this paper. In our calculation, the first, second, and third modes determined by confinement on both leads start at  $E_F = 0.73$  meV, 1.4 meV, and 2.6 meV.

#### A. $K'$ valley

This subsection discusses the transport properties of the  $K'$  valley through the magnetic barrier for the MoS<sub>2</sub> ZNR. The schematic geometry of the magnetic barrier is shown in Fig. 1. In Fig. 3, the conductance of the  $K'$  valley as a function of  $E_F$  is presented for different lengths and strengths of the magnetic barrier.

Figures 3(a)–3(c) show the conductance for different lengths  $L_B$  of the magnetic barrier, ranging from 5 nm to 50 nm in 5 nm increments, at fixed magnetic fields 1 T, 5 T, and 9 T, respectively. In Fig. 3(a), the conductance at a magnetic field of 1 T decreases monotonically as  $L_B$  increases. In Fig. 3(b), for the conductance at a magnetic field of 5 T, the smaller  $L_B$  has a weaker effect on the conductance. In addition, owing to the small length  $L_B$ , there is a tunneling probability that electrons move across the magnetic barrier as in the case of a 1D conventional potential barrier. However, as the length  $L_B$  increases, the conductance starts to be more strongly

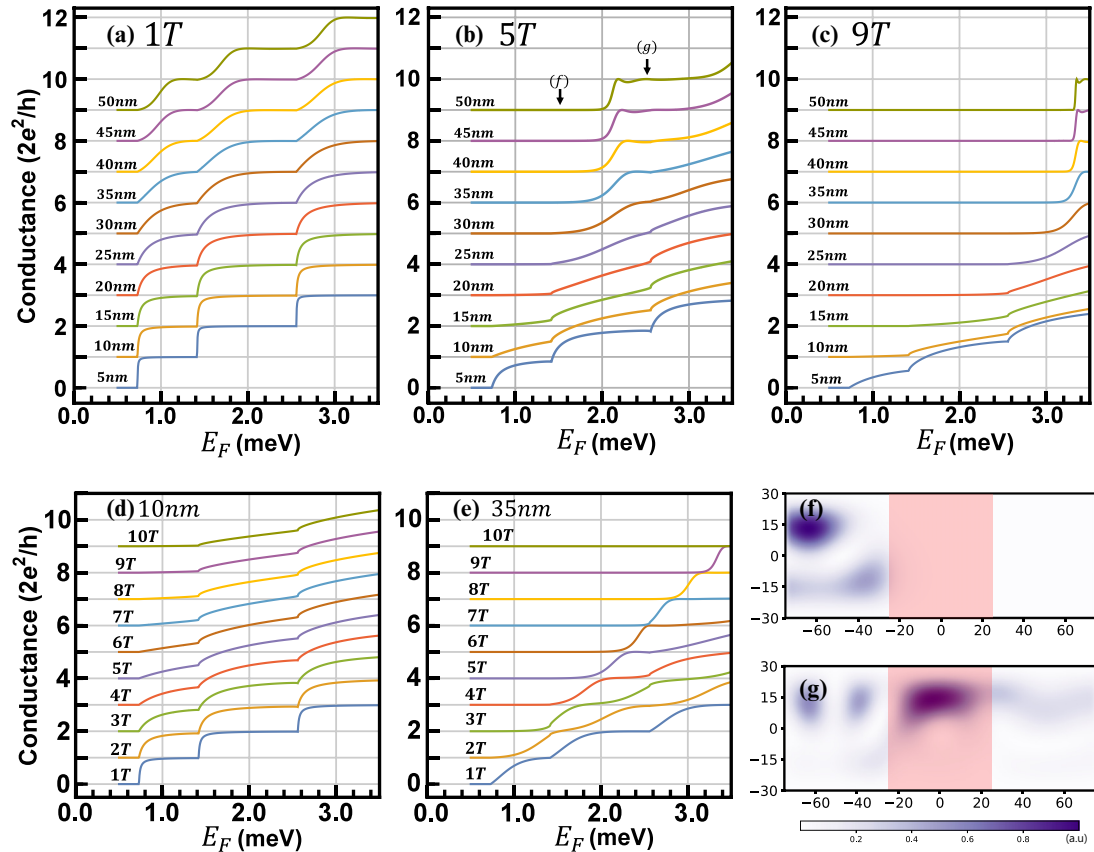


FIG. 3. (a)–(c) Conductance of the  $K'$  valley for a  $\text{MoS}_2$  zigzag nanoribbon as a function of Fermi energy ( $E_F = E_{3\text{band}} - 1.5975$  eV). Each line is for various values of  $L_B$  from 5 nm to 50 nm with an increment of 5 nm for magnetic barrier strengths of 1 T, 5 T, and 9 T, respectively. (d), (e) Conductance for various magnetic fields from 1 T to 10 T with fixed  $L_B = 10$  nm and 35 nm, respectively. Note that each line with different parameters is vertically shifted from the blue line to show the different trends. (f), (g) Probability density profile with  $L_B = 50$  nm and  $B = 5$  T for two different energies  $E = 1.5$  meV and 2.5 meV, respectively. The reddish shading indicates the single magnetic barrier regions.

suppressed. For instance, above  $L_B = 35$  nm, the conductance is completely suppressed below 2.0 meV, and there are clear plateaus where the conductance becomes constant. This step-wise behavior in conductance becomes clear as  $L_B$  increases. This means that an electron cannot move across the magnetic barrier via the tunneling process when its energy is below the zeroth LL. For the cases where there is suppression ( $E_F = 1.5$  meV) or a plateau ( $E_F = 2.5$  meV) in the conductance data for  $L_B = 50$  nm, we plot their local densities in Figs. 3(f) and 3(g), respectively. Figure 3(f) shows that the electron wave function in the  $K'$  valley cannot penetrate the magnetic barrier and is totally reflected. However, Fig. 3(g) shows that a conduction electron in the  $K'$  valley can be transported from source to drain by means of the edge states of the magnetic barriers. These features are also clearly revealed in the case of a magnetic barrier strength of 9 T in Fig. 3(c).

The conductance in the  $K'$  valley for various magnetic fields from 1 T to 10 T with two fixed values of  $L_B$  (10 nm and 35 nm) is shown in Figs. 3(d) and 3(e). For small  $L_B = 10$  nm, the conductance decreases monotonically as the magnetic field increases. On the other hand, in the case of  $L_B = 35$  nm, as the magnetic field increases, the conductance suppression regions are broadened. The energy with which an electron can start to penetrate through the barrier increases. These features are related to the LLs. As the magnetic field of the barrier

increases, the zeroth LL increases, which means that the edge channel energy also increases. If the incident energy is below the zeroth LL, there is no channel through which an electron can penetrate the barrier. Therefore, an electron will experience strong backscattering, which causes a reduction in conductance. However, if a  $K'$  valley electron has an energy above a certain LL, it can move to the drain via possible edge channels. In this case, the conductance exhibits a plateau (quantum Hall effect). These LLs of the magnetic barrier could play a role as a potential barrier against electrons in the  $K'$  valley. In view of the conventional potential barrier, for the  $K'$  valley, as  $L_B$  becomes shorter, the possibility of penetration through the barrier increases, whereas if  $L_B$  becomes longer, the conductance begins to be suppressed except for the edge channel.

### B. $K$ valley

In this subsection, the transport properties of the  $K$  valley through the magnetic barrier for the  $\text{MoS}_2$  ZNR are discussed. Figure 4 shows the conductance of the  $K$  valley for different lengths and strengths of the magnetic barrier. Compared with the conductance of the  $K'$  valley as a function of  $E_F$ , which exhibits simple plateaus, that of the  $K$  valley has a more complex structure. The conductance of the  $K$  valley is shown in Figs. 4(a) and 4(b) for different magnetic fields from 1 T

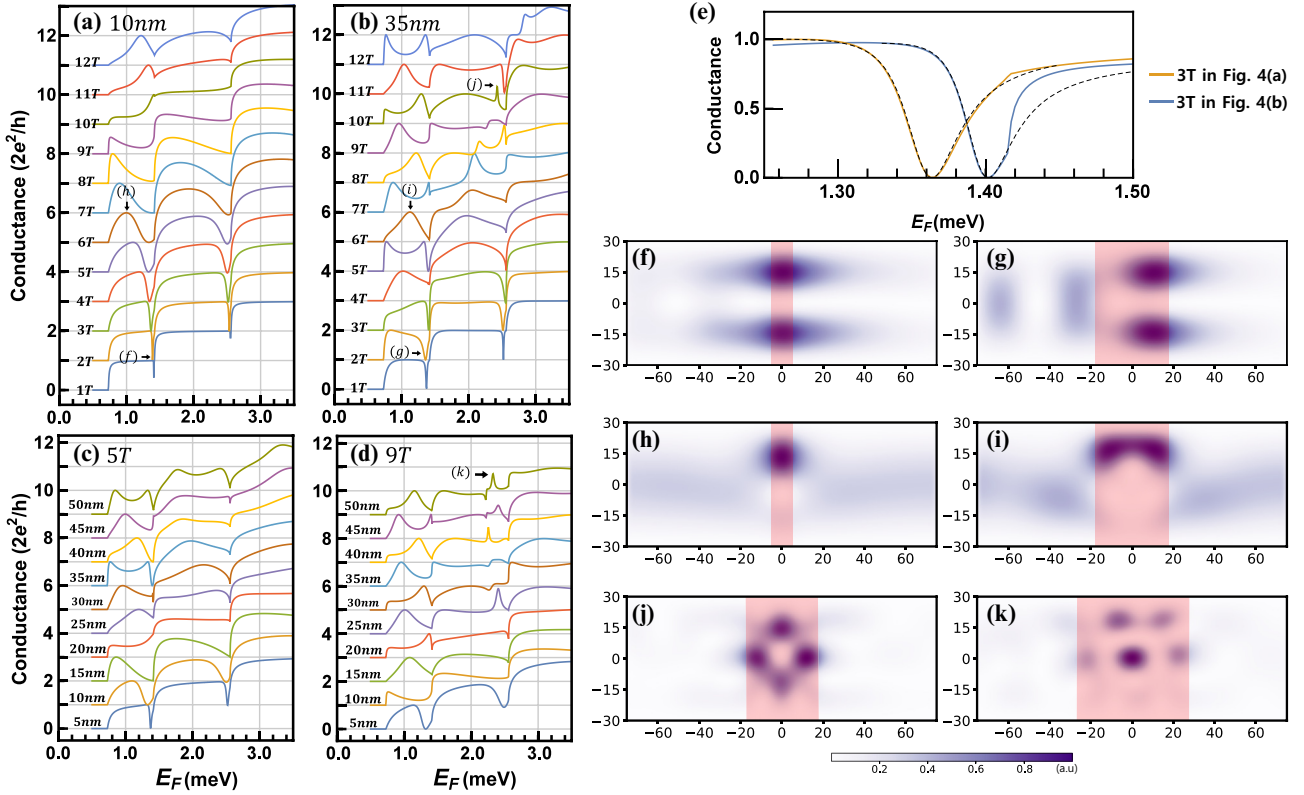


FIG. 4. (a)–(d) Conductance of the  $K$  valley as a function of Fermi energy for fixed  $L_B$  of (a) 10 nm and (b) 35 nm and for fixed strengths of the magnetic barrier of (c) 5 T and (d) 9 T. Note that each line with different parameters is vertically shifted from the blue line to show the different trends. (e) Conductance near Fano resonance dips for 3 T in (a) and (b). To show the Fano resonance, the conductance for the  $n = 0$  mode in the leads is represented. The black dashed lines are fitted lines based on Eq. (9). (f)–(k) Probability density profiles at different values of  $B$ ,  $L_B$ ,  $\epsilon$ : (f) 2 T, 10 nm, 1.39 meV; (g) 2 T, 35 nm, 1.39 meV; (h) 6 T, 10 nm, 1.0 meV; (i) 6 T, 35 nm, 1.11 meV; (j) 10 T, 35 nm, 2.42 meV; (k) 9 T, 50 nm, 2.32 meV. These are indicated by the black arrows and corresponding labels in the conductance graphs. The reddish shading indicates the single magnetic barrier regions.

to 12 T and two fixed values of  $L_B$  (10 nm and 35 nm, respectively). For magnetic fields from 1 T to 3 T, one of the characteristics that can be seen is the presence of strong dips in conductance before the new channels in the source start at 1.42 meV ( $n = 1$ ) and 2.6 meV ( $n = 2$ ), respectively. At these conductance dips for 10 nm and 35 nm, the probability densities are as shown in Figs. 4(f) and 4(g), respectively. These conductance dips are caused by strong backscattering due to the interaction between continuum states and quasi-bound states arising from the valley Zeeman effect. This type of resonance is called Fano resonance [49] and can be expressed as

$$T(\epsilon) \propto \frac{|\epsilon + q|^2}{\epsilon^2 + 1}, \quad (9)$$

where  $\epsilon = (E_F - E_i)/(\Gamma/2)$ , and  $E_i$  and  $\Gamma$  are the resonance energy and width of quasibound states, respectively.  $q$  is the asymmetry parameter and is related to interaction between the continuum and quasibound states. Figure 4(e) shows that fitted lines based on Eq. (9) match the numerical results well around the dip region. However, Fig. 4(e) shows that the intersubband interaction causes the conductance curve to deviate from the fitted line above 1.42 meV, where the second channel in the leads starts to be involved. These resonance dips can also be seen in other systems, such as the Fano–Rashba effect

[41–44], Fano resonance in a general quasi-1D system with local potentials [50], and quantum dots [51,52].

Moreover, in Fig. 4(a), the positions of these conductance dips are shifted as the magnetic barrier strength increases. As the magnetic field increases, the energy bands or LLs for the  $K$  valley in the barrier region become lower, owing to the valley Zeeman effect. In view of the elementary potential well in a quasi-1D problem [50], lowering of LLs should be considered as the depth of potential well increases. Therefore, we can deduce that the Fano resonance energy causing backscattering becomes lower as the magnetic strength increases. As well as the position of the Fano resonance dips, their widths also become broader as the magnetic barrier strength increases.

Taking account of Fano resonance, we can see that magnetic edge states in the magnetic barrier can contribute to conductance. Before the first Fano resonance starts to occur, there is a conductance peak from 1 T to 9 T in Fig. 4(a). The edge state in the barrier region is responsible for these peaks. For instance, Figs. 4(h) and 4(i) show these edge states, whose energy is marked by the black arrows in Figs. 4(a) and 4(b), respectively. As the magnetic field increases further, the LLs in the magnetic barrier become lower, and so the other edge modes start to play a role in conductance. Therefore, above 9 T in Fig. 4(a), even though Fano resonance occurs, the conductance is not suppressed totally, owing to edge modes

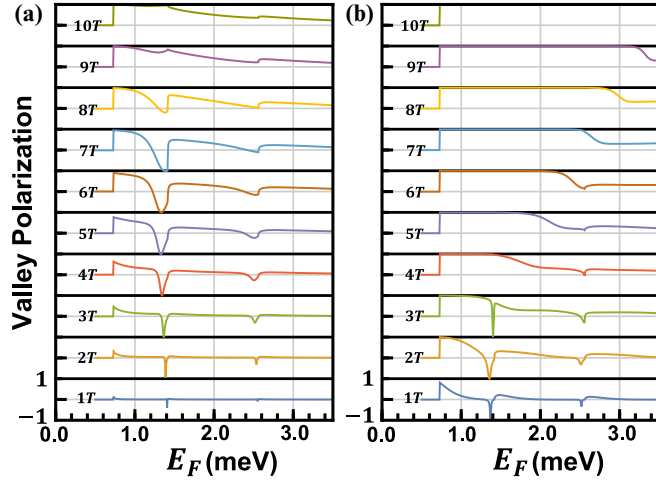


FIG. 5. Valley polarization due to magnetic barriers with (a)  $L_B = 10$  nm and (b)  $L_B = 35$  nm, with 1 T increments of the magnetic field from 1 T to 10 T. Polarizations of +1 and -1 correspond to perfectly polarized  $K$  and  $K'$  states, respectively.

corresponding to higher LLs. Also, from 10 T to 12 T, there is another conductance peak in which edge states in higher LLs are involved. Therefore, depending on the strength of the magnetic field, owing to Fano resonance and edge states, the conductance exhibits repeated increasing and decreasing trends. In Fig. 4(b), this oscillation in conductance becomes clearer. It can be seen that the size of the magnetic barrier has an effect on its quasibound states.

Figures 4(c) and 4(d) show the conductance in the  $K$  valley as  $L_B$  increases from 5 nm to 50 nm in 5 nm increments at fixed magnetic fields of 5 T and 9 T, respectively. In these cases, the width of the conductance dip increases as  $L_B$  increases. The generic features are similar to what is seen in Figs. 4(a) and 4(b).

In addition, in the conductance in the  $K$  valley, there are several transmission peaks that cannot be seen in the case of the  $K'$  valley, for instance, the two peaks marked by black arrows and labeled (j) and (k) in Figs. 4(b) and 4(d). The probability densities at these peaks are shown in Figs. 4(j) and 4(k), respectively. Unlike strong backscattering due to Fano resonance, electrons can move across the barrier via resonant tunneling caused by localized states of the magnetic barrier.

### C. Spin and valley polarizations

Based on the features of the  $K$  and  $K'$  valleys in the  $\text{MoS}_2$  ZNR, we consider spin and valley polarizations in this subsection. The spin polarization  $P_s$  and valley polarization  $P_v$  are defined as follows:

$$P_s = \frac{G_{K\uparrow} - G_{K\downarrow} + G_{K'\uparrow} - G_{K'\downarrow}}{G_{K\uparrow} + G_{K\downarrow} + G_{K'\uparrow} + G_{K'\downarrow}}, \quad (10)$$

$$P_v = \frac{G_{K\uparrow} + G_{K\downarrow} - G_{K'\uparrow} - G_{K'\downarrow}}{G_{K\uparrow} + G_{K\downarrow} + G_{K'\uparrow} + G_{K'\downarrow}}, \quad (11)$$

where  $G_{a,b}$  is the conductance of the system,  $a \in (K, K')$ , and  $b \in (\uparrow, \downarrow)$ .

First, Fig. 5 shows the valley polarization of  $\text{MoS}_2$  for two different magnetic barrier lengths. Values of +1 and

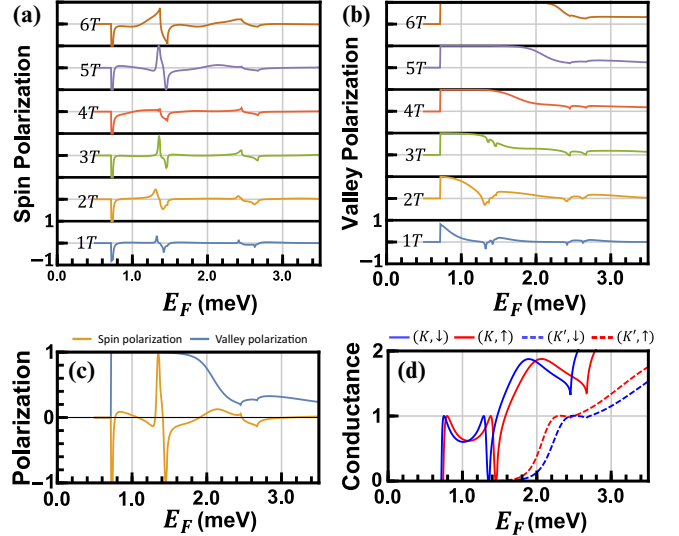


FIG. 6. (a) Spin polarization and (b) valley polarization of an  $\text{MoS}_2$  ZNR with  $L_B = 35$  nm for six different magnetic barrier strengths. (c) Spin polarization for 5 T and 35 nm. (d) Conductance for different valleys and spins for 5 T and 35 nm.

-1 indicate fully polarized  $K$  and  $K'$  valleys, respectively. For simplicity, we do not consider the intrinsic SOI in this figure. In general, for both cases, in the low-energy range below 1.2 meV, systems are almost entirely polarized in the  $K$  valley. However, when the incident energy becomes close to about 1.4 meV, where Fano resonance occurs, the valley polarization is switched from  $K$  to  $K'$ . For the case of  $L_B = 10$  nm [Fig. 5(a)], as the magnetic strength increases to 8 T, the energy range, with the  $K'$  valley having become fully polarized, becomes broader, and above this magnetic field, the dip starts to disappear. At energies higher than 1.4 meV, the valley polarization goes to zero, owing to mixing between valleys.

For the other case of  $L_B = 35$  nm [Fig. 5(b)], it is the  $K$  valley that is fully polarized over a large energy range as the magnetic field increases. This reflects the fact that conduction electrons in the  $K'$  valley can penetrate the magnetic barrier less easily than those in the  $K$  valley, as discussed in Sec. III A. The results show that if  $L_B$  is sufficiently large, the electrons in the  $K'$  valley cannot penetrate the magnetic barrier, and the width of the Fano resonance in the  $K$  valley becomes narrower, which makes it difficult to manipulate the valley polarization. Therefore, for switching valley polarization in our system, a relatively small  $L_B$  is preferred, so there is nonzero conductance for the  $K'$  valley at the conductance dip of the  $K$  valley. For instance, in Fig. 5(a), at  $B = 7$  T, the valley polarization is switched from  $K$  to  $K'$  between  $E = 0.85$  meV and  $E = 1.40$  meV. Thus, by manipulating the strength and length of the magnetic barrier, it is possible to find an energy range where the valley polarization can be switched from  $K$  to  $K'$  without changing the direction of the magnetic field.

In Fig. 6, the spin polarization and valley polarization of  $\text{MoS}_2$  ZNR with  $L_B = 35$  nm are presented for six different magnetic barrier strengths. In this case, the intrinsic SOI has been taken into account to reveal its detailed behavior. For small magnetic barrier lengths, the general features are the same as in the absence of SOI. Figure 6(a) shows the

system's spin polarization, which is close to zero in most energy regions for the different magnetic fields. However, there is strong spin polarization near 0.7 meV and 1.4 meV, where the Fano resonance occurs. In Fig. 6(b), it can be seen that the valley polarization is initially confined to the  $K$  valley and then approaches zero. For the six different magnetic fields, the spin polarization and valley polarization for 5 T are compared alongside one another in Fig. 6(c). It can be seen that near 1.4 meV, spin-up polarization switches rapidly into spin-down polarization in the  $K$  valley. To examine this further, the conductances from the different spin and valley components are presented in Fig. 6(d). On the one hand, the valley Zeeman effect suppresses the  $K'$  valley conductance until the energy reaches about 1.8 meV. On the other hand, it is possible for each spin component to become fully polarized, owing to spin splitting and Fano resonance. These results show that for a magnetic field barrier of 5 T and length 35 nm, the spin polarization can be changed from spin-up to spin-down entirely near 1.4 meV, where the conductance is purely  $K$  valley. In addition, if we change the direction of the magnetic field, spin-up and spin-down polarization of the  $K'$  valley can be obtained in the same energy region. Thus, four distinct spin and valley components can be obtained by manipulating the direction and strength of the magnetic field.

#### IV. CONCLUSION

In summary, we have shown that spin and valley polarization can be achieved in a MoS<sub>2</sub> ZNR with a magnetic barrier,

as a result of strong intervalley backscattering caused by Fano resonance. Owing to the valley Zeeman effect, electrons in the  $K$  and  $K'$  valleys behave differently in the magnetic field barrier region. The energy dispersion, conductance, and local probability density have been investigated to reveal the details of transport in the different valleys. In the presence of the magnetic barrier, the  $K'$  valley exhibits simple plateaus in conductance, resulting from magnetic edge states. On the other hand, the  $K$  valley has a more complex conductance structure, caused by magnetic edge states and LL states in the magnetic barrier, which result in strong backscattering in conductance dips. These conductance dips play an important role in achieving a highly valley-polarized current. Because the broadness of the Fano resonance deep in the  $K$  valley can be manipulated by changing the width and strength of the magnetic barrier, optimized conditions for spin and valley polarizations can be found. The results presented here provide a useful basis for the development of devices employing spin- and valley-polarized currents.

#### ACKNOWLEDGMENTS

This work was supported by the Basic Science Research Program through the National Research Foundation of Korea (NRF) and was funded by the Ministry of Science and ICT (Grant No. NRF-2019R1A2C1088327).

The authors declare that they have no known competing financial interests or personal relationships that could influence the work reported in this paper.

- 
- [1] A. H. Castro Neto, F. Guinea, N. M. R. Peres, K. S. Novoselov, and A. K. Geim, *Rev. Mod. Phys.* **81**, 109 (2009).
  - [2] D. Xiao, G.-B. Liu, W. Feng, X. Xu, and W. Yao, *Phys. Rev. Lett.* **108**, 196802 (2012).
  - [3] B. Radisavljevic and A. Kis, *Nat. Mater.* **12**, 815 (2013).
  - [4] H. Li, Z. Yin, Q. He, H. Li, X. Huang, G. Lu, D. W. H. Fam, A. I. Y. Tok, Q. Zhang, and H. Zhang, *Small* **8**, 63 (2012).
  - [5] Z. Yin, H. Li, H. Li, L. Jiang, Y. Shi, Y. Sun, G. Lu, Q. Zhang, X. Chen, and H. Zhang, *ACS Nano* **6**, 74 (2012).
  - [6] Y.-Z. Chen, S.-W. Wang, C.-C. Yang, C.-H. Chung, Y.-C. Wang, S.-W. Huang Chen, C.-W. Chen, T.-Y. Su, H.-N. Lin, H.-C. Kuo, and Y.-L. Chueh, *Nanoscale* **11**, 10410 (2019).
  - [7] K. F. Mak, C. Lee, J. Hone, J. Shan, and T. F. Heinz, *Phys. Rev. Lett.* **105**, 136805 (2010).
  - [8] K. K. Kam and B. A. Parkinson, *J. Phys. Chem.* **86**, 463 (1982).
  - [9] Z. Y. Zhu, Y. C. Cheng, and U. Schwingenschlögl, *Phys. Rev. B* **84**, 153402 (2011).
  - [10] H.-Z. Lu, W. Yao, D. Xiao, and S.-Q. Shen, *Phys. Rev. Lett.* **110**, 016806 (2013).
  - [11] K. F. Mak, K. L. McGill, J. Park, and P. L. McEuen, *Science* **344**, 1489 (2014).
  - [12] D. Xiao, W. Yao, and Q. Niu, *Phys. Rev. Lett.* **99**, 236809 (2007).
  - [13] W. Yao, D. Xiao, and Q. Niu, *Phys. Rev. B* **77**, 235406 (2008).
  - [14] T. Cao, G. Wang, W. Han, H. Ye, C. Zhu, J. Shi, Q. Niu, P. Tan, E. Wang, B. Liu, and J. Feng, *Nat. Commun.* **3**, 887 (2012).
  - [15] J. R. Schaibley, H. Yu, G. Clark, P. Rivera, J. S. Ross, K. L. Seyler, W. Yao, and X. Xu, *Nat. Rev. Mater.* **1**, 16055 (2016).
  - [16] Y. P. Shkolnikov, E. P. De Poortere, E. Tutuc, and M. Shayegan, *Phys. Rev. Lett.* **89**, 226805 (2002).
  - [17] H. Rostami and R. Asgari, *Phys. Rev. B* **91**, 075433 (2015).
  - [18] S. Wu, J. S. Ross, G.-B. Liu, G. Aivazian, A. Jones, Z. Fei, W. Zhu, D. Xiao, W. Yao, D. Cobden, and X. Xu, *Nat. Phys.* **9**, 149 (2013).
  - [19] Y. Ye, J. Xiao, H. Wang, Z. Ye, H. Zhu, M. Zhao, Y. Wang, J. Zhao, X. Yin, and X. Zhang, *Nat. Nanotechnol.* **11**, 598 (2016).
  - [20] J. Lee, Z. Wang, H. Xie, K. F. Mak, and J. Shan, *Nat. Mater.* **16**, 887 (2017).
  - [21] O. Gunawan, Y. P. Shkolnikov, K. Vakili, T. Gokmen, E. P. De Poortere, and M. Shayegan, *Phys. Rev. Lett.* **97**, 186404 (2006).
  - [22] H. Zeng, J. Dai, W. Yao, D. Xiao, and X. Cui, *Nat. Nanotechnol.* **7**, 490 (2012).
  - [23] K. F. Mak, K. He, J. Shan, and T. F. Heinz, *Nat. Nanotechnol.* **7**, 494 (2012).
  - [24] H. Li, J. Shao, D. Yao, and G. Yang, *ACS Appl. Mater. Interfaces* **6**, 1759 (2014).
  - [25] R.-Y. Yuan, Q.-J. Yang, and Y. Guo, *J. Phys.: Condens. Matter* **30**, 355301 (2018).
  - [26] Y. Hajati, Z. Amini, and M. Sabaeian, *J. Magn. Magn. Mater.* **503**, 166580 (2020).
  - [27] B. Liu, D. Liu, R. Yuan, and Y. Guo, *J. Phys. D: Appl. Phys.* **54**, 425305 (2021).

- [28] R. Liu, G. Hu, M. Dan, Y. Zhang, L. Li, and Y. Zhang, *Nano Energy* **72**, 104678 (2020).
- [29] X. J. Qiu, Z. Z. Cao, Y. F. Cheng, and C. C. Qin, *J. Phys.: Condens. Matter* **29**, 105301 (2017).
- [30] L. Majidi and R. Asgari, *Phys. Rev. B* **90**, 165440 (2014).
- [31] L. Majidi, H. Rostami, and R. Asgari, *Phys. Rev. B* **89**, 045413 (2014).
- [32] W.-T. Lu, H.-Y. Tian, H.-M. Liu, Y.-F. Li, and W. Li, *Phys. Rev. B* **98**, 075405 (2018).
- [33] D. MacNeill, C. Heikes, K. F. Mak, Z. Anderson, A. Kormányos, V. Zólyomi, J. Park, and D. C. Ralph, *Phys. Rev. Lett.* **114**, 037401 (2015).
- [34] G. Aivazian, Z. Gong, A. M. Jones, R.-L. Chu, J. Yan, D. G. Mandrus, C. Zhang, D. Cobden, W. Yao, and X. Xu, *Nat. Phys.* **11**, 148 (2015).
- [35] A. Srivastava, M. Sidler, A. V. Allain, D. S. Lembke, A. Kis, and A. Imamoglu, *Nat. Phys.* **11**, 141 (2015).
- [36] Y. Li, J. Ludwig, T. Low, A. Chernikov, X. Cui, G. Arefe, Y. D. Kim, A. M. van der Zande, A. Rigosi, H. M. Hill, S. H. Kim, J. Hone, Z. Li, D. Smirnov, and T. F. Heinz, *Phys. Rev. Lett.* **113**, 266804 (2014).
- [37] R.-L. Chu, X. Li, S. Wu, Q. Niu, W. Yao, X. Xu, and C. Zhang, *Phys. Rev. B* **90**, 045427 (2014).
- [38] A. Ueda, I. Baba, K. Suzuki, and M. Eto, *J. Phys. Soc. Jpn.* **72**, 157 (2003).
- [39] J. Barański, T. Zienkiewicz, M. Barańska, and K. J. Kapcia, *Sci. Rep.* **10**, 2881 (2020).
- [40] H.-Y. Mu, N.-W. Wang, Y.-N. Du, X.-T. An, and J.-J. Liu, *Phys. Rev. B* **105**, 115305 (2022).
- [41] D. Sánchez and L. Serra, *Phys. Rev. B* **74**, 153313 (2006).
- [42] D. H. Park, H. Kim, and N. Kim, *Phys. Status Solidi (b)* **256**, 1800619 (2019).
- [43] R. Lima, J. Bautista, and P. Orellana, *Physica E* **114**, 113618 (2019).
- [44] Y. S. Liu, X. K. Hong, J. F. Feng, and X. F. Yang, *Nanoscale Res. Lett.* **6**, 618 (2011).
- [45] G.-B. Liu, W.-Y. Shan, Y. Yao, W. Yao, and D. Xiao, *Phys. Rev. B* **88**, 085433 (2013).
- [46] E. S. Kadantsev and P. Hawrylak, *Solid State Commun.* **152**, 909 (2012).
- [47] S. Lebègue and O. Eriksson, *Phys. Rev. B* **79**, 115409 (2009).
- [48] C. W. Groth, M. Wimmer, A. R. Akhmerov, and X. Waintal, *New J. Phys.* **16**, 063065 (2014).
- [49] A. E. Miroshnichenko, S. Flach, and Y. S. Kivshar, *Rev. Mod. Phys.* **82**, 2257 (2010).
- [50] E. Tekman and P. F. Bagwell, *Phys. Rev. B* **48**, 2553 (1993).
- [51] K. Kobayashi, H. Aikawa, S. Katsumoto, and Y. Iye, *Phys. Rev. Lett.* **88**, 256806 (2002).
- [52] F. Chi, J.-L. Liu, and L.-L. Sun, *J. Appl. Phys.* **101**, 093704 (2007).